Classifying Microwave Radiometer Observations over the Netherlands into Dry, Shallow, and Nonshallow Precipitation Using a Random Forest Model

Bogerd, Linda; Kidd, Chris; Kummerow, Christian; Leijnse, Hidde; Overeem, Aart; Petkovic, Veljko; Whan, Kirien; Uijlenhoet, Remko

DOI
10.1175/JHM-D-23-0202.1

Publication date
2024

Document Version
Final published version

Published in
Journal of Hydrometeorology

Citation (APA)
Bogerd, L., Kidd, C., Kummerow, C., Leijnse, H., Overeem, A., Petkovic, V., Whan, K., & Uijlenhoet, R. (2024). Classifying Microwave Radiometer Observations over the Netherlands into Dry, Shallow, and Nonshallow Precipitation Using a Random Forest Model. *Journal of Hydrometeorology*, *25*(6), 881-898. https://doi.org/10.1175/JHM-D-23-0202.1

Classifying Microwave Radiometer Observations over the Netherlands into Dry, Shallow, and Nonshallow Precipitation Using a Random Forest Model

LINDA BOGERD,[a,b] CHRIS KIDD,[c] CHRISTIAN KUMMEROW,[d] HIDDE LEIJNSE,[b] AART OVEREEM,[b,e] VELJKO PETKOVIC,[f] KIRIEN WHAN,[b] AND REMKO UIJLENHOET[e]

[a] *Hydrology and Environmental Hydraulics Group, Wageningen University and Research, Wageningen, Netherlands*
[b] *R&D Observations and Data Technology, Royal Netherlands Meteorological Institute (KNMI), De Bilt, Netherlands*
[c] *NASA Goddard Space Flight Center, Greenbelt, Maryland*
[d] *Department of Atmospheric Science, Colorado State University, Fort Collins, Colorado*
[e] *Department of Water Management, Faculty of Civil Engineering and Geosciences, Delft University of Technology, Delft, Netherlands*
[f] *Earth System Science Interdisciplinary Center, University of Maryland, College Park, College Park, Maryland*

(Manuscript received 17 November 2023, in final form 15 February 2024, accepted 20 March 2024)

ABSTRACT: Spaceborne microwave radiometers represent an important component of the Global Precipitation Measurement (GPM) mission due to their frequent sampling of rain systems. Microwave radiometers measure microwave radiation (brightness temperatures Tb), which can be converted into precipitation estimates with appropriate assumptions. However, detecting shallow precipitation systems using spaceborne radiometers is challenging, especially over land, as their weak signals are hard to differentiate from those associated with dry conditions. This study uses a random forest (RF) model to classify microwave radiometer observations as dry, shallow, or nonshallow over the Netherlands—a region with varying surface conditions and frequent occurrence of shallow precipitation. The RF model is trained on five years of data (2016–20) and tested with two independent years (2015 and 2021). The observations are classified using ground-based weather radar echo top heights. Various RF models are assessed, such as using only GPM Microwave Imager (GMI) Tb values as input features or including spatially aligned ERA5 2-m temperature and freezing level reanalysis and/or Dual-Frequency Precipitation Radar (DPR) observations. Independent of the input features, the model performs best in summer and worst in winter. The model classifies observations from high-frequency channels (≥85 GHz) with lower Tb values as nonshallow, higher values as dry, and those in between as shallow. Misclassified footprints exhibit radiometric characteristics corresponding to their assigned class. Case studies reveal dry observations misclassified as shallow are associated with lower Tb values, likely resulting from the presence of ice particles in nonprecipitating clouds. Shallow footprints misclassified as dry are likely related to the absence of ice particles.

SIGNIFICANCE STATEMENT: Published research concerning rainfall retrieval algorithms from microwave radiometers is often focused on the accuracy of these algorithms. While shallow precipitation over land is often characterized as problematic in these studies, little progress has been made with these systems. In particular, precipitation formed by shallow clouds, where shallow refers to the clouds being close to Earth's surface, is often missed. This study is focused on detecting shallow precipitation and its physical characteristics to further improve its detection from spaceborne sensors. As such, it contributes to understanding which shallow precipitation scenes are challenging to detect from microwave radiometers, suggesting possible ways for algorithm improvement.

KEYWORDS: Precipitation; Satellite observations; Machine learning

1. Introduction

The intensification of the water cycle due to global warming (Held and Soden 2006; Huntington 2006) is expected to increase the frequency of droughts and extreme rainfall events (IPCC 2021). The consequences can be reduced through adaptation and mitigation measures, but these require long-term forecast models, which in turn require accurate observations of precipitation on a global scale. Unfortunately, coverage from ground-based precipitation measurements is limited (Lorenz and Kunstmann 2012; Saltikoff et al. 2019) in locations where the impact of the intensified water cycle is expected to be large (Nath and Behera 2011; Winsemius et al. 2018; IPCC 2022). Precipitation estimates derived from spaceborne sensors with global coverage can complement ground-based sensors. However, precipitation estimates derived from space-based sensors are not of the same quality as those from ground-based sensors (Chen and Li 2016; Shen et al. 2020; Tang et al. 2020; Maggioni et al. 2022). Understanding the origins of this reduced quality for each sensor type is crucial to improving satellite-based estimates.

Many studies have focused on improving estimates retrieved from spaceborne microwave radiometers (e.g., Petty and Li 2013;

Denotes content that is immediately available upon publication as open access.

Supplemental information related to this paper is available at the Journals Online website: https://doi.org/10.1175/JHM-D-23-0202.s1.

Corresponding author: Linda Bogerd, linda.bogerd@wur.nl

DOI: 10.1175/JHM-D-23-0202.1

Shige et al. 2013; Klotz and Uhlhorn 2014; Yamamoto et al. 2017; Petković et al. 2018, 2019). Compared to better-performing spaceborne radars, microwave radiometers are often the preferred sensor for precipitation because they are less costly and their swath is typically wider (for instance, shown in Fig. 2 from Hou et al. 2014), resulting in better coverage of Earth's surface. Both radars and microwave radiometers are only available on low-Earth-orbiting satellites that, due to their swaths, have gaps between adjacent observations. While visible (VIS) and infrared (IR) channels with good spatial resolution are available on both low-Earth-orbiting and geostationary satellites, only the latter provides frequent and regular temporal sampling.

Sensors with VIS and IR channels only observe cloud top properties that are used to indirectly estimate surface precipitation intensities (e.g., Levizzani et al. 2001; Behrangi et al. 2009; Kidd and Levizzani 2011). Hence, the uncertainty and inaccuracy of spaceborne precipitation estimates derived from VIS/IR observations are larger than those derived from spaceborne radar and microwave radiometer observations (Lee et al. 2015; Iwabuchi et al. 2016; Maggioni et al. 2022).

Radiometers measure the microwave radiation emitted by Earth's surface and other natural sources such as clouds and precipitation particles (Kummerow and Giglio 1994; Maggioni et al. 2016; Kummerow 2020; Kidd et al. 2021). Water drops absorb and emit this radiation at their own thermal temperature, often increasing the observed microwave radiation (expressed as brightness temperatures Tb) compared to the same situation without rainfall. This interaction between radiation and raindrops is exploited over areas with a constant and radiatively cold temperature (hence low emissivity), such as oceans (Wilheit et al. 1977; Spencer 1986; Kummerow and Giglio 1994). Over land, the background surface emissivity is higher, and detecting emissions due to water drops is more challenging due to the greater variability in the background caused by changes in the surface type and water content. Variation in surface type mostly affects the observations of the lower-frequency channels. Retrieval schemes over land are therefore often based on the higher-frequency channels (≥85 GHz), which rely on temperature depressions due to the scattering of upwelling radiation caused by ice particles often present during precipitation (Wilheit et al. 1982; Kummerow and Giglio 1994; McCollum et al. 2002; Kummerow 2020).

However, microwave radiometers measure radiation from the surface and along the vertical column of the intervening atmosphere. Consequently, radiometers cannot identify the height of the radiation source. In addition, a combination of Tb values retrieved from various channels could yield multiple solutions when converting these Tb values into precipitation intensities (Anagnostou 2004; Kummerow et al. 2011; Kidd et al. 2018; Kummerow 2020). Some precipitation regimes, such as warm rain, have a limited scattering signal due to the absence of ice (Liu and Zipser 2009; Adhikari et al. 2019), resulting in a weak radiometric signature from light or shallow precipitation close to Earth's surface (Lin and Hou 2012; You et al. 2020; Hayden and Liu 2021). As a consequence, warm, light, and shallow precipitation are often missed by microwave radiometers (Behrangi et al. 2014; Adhikari and Behrangi 2022) over land surfaces.

A recent effort to improve the detection and accuracy of light and shallow precipitation estimates observed by spaceborne microwave radiometers is the Global Precipitation Measurement (GPM) mission (Hou et al. 2014; Skofronick-Jackson et al. 2018). GPM consists of a constellation of satellites with radiometers aboard and a core-satellite carrying both a radiometer [the GPM Microwave Imager (GMI)] and a radar [the Dual-Frequency Precipitation Radar (DPR)]. The combination of simultaneous radiometer and radar observations provides the opportunity to study coupled Tb and vertical precipitation structures to better constrain the retrieval schemes that convert Tb values to precipitation estimates (e.g., Kummerow et al. 2015; Panegrossi et al. 2020; Tiberia et al. 2021; D'Adderio et al. 2022).

Despite the capabilities of the DPR, it has limited capabilities to detect shallow and light precipitation and, if detected, to accurately measure the intensity (Arulraj and Barros 2017; Casella et al. 2017; Watters et al. 2018; Liao and Meneghini 2019; Bogerd et al. 2024). Due to surface clutter, the DPR cannot retrieve near-surface precipitation below about 1000 m at the nadir, increasing to about 1500 m at the outer scans of the DPR due to the slanted angle of observation (Awaka et al. 2016; Hirose et al. 2021). The lack of these observations inevitably results in missing some shallow precipitation. Coupling a high-quality ground-based reference is a better way to increase our understanding of the behavior of Tb values during shallow precipitation events. Furthermore, exploiting the GMI's entire swath instead of only the scans matched with the DPR increases the extent of the region covered.

Here, we implement a random forest (RF) model to determine the extent to which nonrainy conditions (referred to as dry in the remainder of this paper) and shallow and nonshallow precipitation can be classified from microwave radiometer observations and to gain an understanding of the characteristics of misclassified observations. The focus of this study is to understand observations associated with shallow precipitation and not necessarily to improve their precipitation estimates. Each footprint is classified using a high-quality echo top height (ETH) dataset based on two radars located in the Netherlands. This country is a highly suitable research area due to the frequent occurrence of shallow and light precipitation events, both of which are difficult to detect with spaceborne sensors. Five years of data (2016–20) are used to train the RF model, and data from two independent years (2015 and 2021) are used as test data. Additionally, ERA5 reanalysis data and some DPR products are used to study whether additional input features improve the RF model.

2. Measurement and methods

a. *Study area: The Netherlands*

The Netherlands (50.78°–53.68°N, 3.38°–7.38°E; ~45 000 km^2) is a small country with low relief. Two ground-based C-band weather radars cover the entire country due to its small size, and beam blockage related to orography is virtually absent. Germany

borders the Netherlands on the east, Belgium on the south, and the North Sea on the west and north. In total, the length of the Dutch coastline is 523 km. The coast hampers radiometer-based precipitation retrieval as the varying background (both land and sea within one footprint) makes the surface emission very difficult to quantify. Additionally, shallow and light precipitation frequently occur over northern locations such as the Netherlands. These two characteristics in combination with high-quality reference data make the Netherlands an ideal location for this research.

1) CLIMATOLOGICAL CHARACTERISTICS

The Netherlands has a temperate maritime climate and experiences a pronounced annual cycle. While the total amount of precipitation is generally distributed evenly throughout the year, precipitation intensity and occurrence vary with season. Winter (DJF) experiences the highest occurrence of shallow and light precipitation, with occasional snowfall. In spring (MAM), precipitation is mostly liquid, and the higher land surface temperatures enable higher precipitation intensities. The high surface temperatures during summer (JJA) result in a larger temperature difference with the colder upper levels of the atmosphere, which in combination with the presence of moist air promote the development of convective systems. Summer has the lowest occurrence of light and shallow rainfall. In fall (SON), both temperatures and rainfall intensities decrease. More information on the Dutch climate can be found in Daniels et al. (2014) and Overeem et al. (2009b). Additionally, Bogerd et al. (2021) analyzed precipitation data (both spaceborne and ground-based) in the Netherlands from 2015 to 2019, overlapping with the current research period.

2) HYDROLOGICAL EXTREMES DURING THE RESEARCH PERIOD

An RF model requires representative training data. Hence, we provide a brief overview of the characteristics of the input data (1 January 2015–31 December 2021). The driest June and July since the start of the Dutch meteorological records occurred in 2018. Spring 2020 (in particular April and May) and December 2016 were exceptionally dry. June 2016, February 2020, and March 2019 were three exceptionally wet months, and November 2015 was wetter than average. Snow occurred in April 2016, February and December 2017, February 2018, January 2019, and January, February, and April 2021. The years 2015 and 2021 were chosen as both experienced a small number of exceptionally wet or dry months, and we are interested in knowing the performance of the model in a "normal" year. The summaries of the weather during all months, seasons, and years can be found at https://www.knmi.nl/nederland-nu/klimatologie/gegevens/mow (in Dutch).

b. Data

1) SATELLITE-BASED DATA

Observations from both the microwave radiometer and radar aboard the GPM core-satellite were selected, and their spatial variables were used as input features. The GPM core-satellite was launched in 2014 and has an orbit between 65°S and 65°N (Hou et al. 2014). The satellite revisits the Netherlands at least once per day.

(i) GPM Microwave Imager

GMI is a radiometer equipped with 13 channels at eight different frequencies. Five frequencies, 10.6, 18.7, 37, 89, and 166 GHz, are horizontally (H) and vertically (V) polarized channels, while the frequencies 23.8, 183 ± 3, and 183 ± 7 GHz are vertically polarized channels. Polarization differences (V − H) can provide information about the radiation source. Large differences are often associated with ocean surfaces, while small differences are often associated with land or hydrometeors (i.e., liquid cloud and precipitation) (Kidd 1998; Cecil and Chronis 2018). In general, the 10.6-, 18.7-, and 23-GHz channels are sensitive to heavy and moderate precipitation; the 37- and 89-GHz channels are sensitive to precipitation mixtures (liquid, ice, and snow); and the 166, 183 ± 3, and 183 ± 7 GHz channels are sensitive to light rain and snowfall. More information about the GMI can be found in Hou et al. (2014), Draper et al. (2015), and Petty and Bennartz (2017).

Tb values from lower-frequency channels were subtracted from those observed by higher-frequency channels to form input parameters of differences in brightness temperatures. Subsequently, the lower-frequency channels were excluded as independent parameters to reduce the number of input parameters. Hence, the lower-frequency observations are indirectly included in all models, while the observations from low-frequency channels are only explicitly included in the "all frequencies (ALL)" model.

In this study, brightness temperatures Tb retrieved from all 13 channels were used as input for the RF model. One GMI scan consists of 221 pixels, but the seven outer pixels of the GMI swath (thus 14 pixels per scan) were removed since the outer pixels are not sampled at the higher frequencies, yielding 207 pixels for each scan line. Higher-frequency channels (≥85 GHz) are emphasized due to the focus on retrievals over land. In addition to the single channels and polarization differences, the differences between three high-frequency (89V, 166V, and 183 ± 7 GHz) and two low-frequency (23.8V and 18.7V) channels were used since combining higher- and lower-frequency channels provides information on both the scattering and emission properties (Wilheit et al. 1994). More combinations were tested but were, due to their limited importance, not included for further analysis.

(ii) GPM DPR

The second instrument aboard the GPM core-satellite is the DPR. This dual-frequency radar operates with a Ku band (13.6 GHz, suitable for heavier rain) and a Ka band (35.5 GHz, suitable for lighter rain and snow). Combining the two bands allows the retrieval of more information regarding the microphysical properties, such as the melting layer and precipitation type (Iguchi et al. 2022). This study used level 2 DPR products, which are either attenuation-corrected reflectivity observations or precipitation characteristics derived from raw observations

TABLE 1. The five RF models evaluated in this study. The "basic" model was evaluated twice: BASIC and IM-BASIC. The other models were only evaluated on a balanced dataset. Henceforth, the models are denoted by their respective abbreviations.

Name	Model	Input features
BASIC	Basic	All frequency channels ≥ 85 GHz
IM-BASIC	Imbalanced basic	BASIC but tested on an imbalanced dataset
ALL	All frequencies	All frequency channels (10–183 GHz)
ERA	Basic + ERA5	Basic plus ERA5 (freezing level, temperature)
ERA + DPR	Basic + ERA5 + DPR	ERA5 plus DPR (flagBB, heightBB, flagShallowRain, precipRateNearSurface)
STORMTOP	Basic + ERA5 + DPR + storm top	ERA5 + DPR plus DPR retrieved storm top height

(level 1). More information about the DPR and associated algorithms to convert DPR's raw observation data to precipitation products or corrected reflectivity profiles can be found in Toyoshima et al. (2015), Iguchi (2020), and Masaki et al. (2020).

The following 2D-DPR products were used as input features: surface precipitation rate (precipRateNearSurface), bright band flag (flagBB), height bright band (heightBB), shallow precipitation flag (flagShallowRain), and storm top height (heightStormTop). DPR's vertical attenuation-corrected reflectivity observations from both the Ka and Ku bands were used to analyze vertical reflectivity profiles. Although DPR's performance is limited for shallow and light precipitation, as mentioned in section 1, its reflectivity observations can yield additional information about (in)correctly classified footprints.

2) REANALYSIS DATA: ERA5 MOISTURE AND TEMPERATURE DATA

Two-meter temperature and freezing level height ERA5 reanalysis data (hourly, 0.25° × 0.25°) were included as additional input features. ERA5 combines real observations (e.g., from radiosondes, aircraft, and satellites) with physics-based model data to generate a global analysis field. More information about ERA5 and the models it employs can be found in Hoffmann et al. (2019), Hersbach et al. (2020), and Muñoz-Sabater et al. (2021). ERA5 is used as it is also implemented in GPROF's scheme that generates precipitation estimates from the GPM Tb values (Randel et al. 2020).

3) GROUND-BASED DATA: ETHS AND PRECIPITATION INTENSITIES

The ground-based radars mentioned in section 2a and their products are operated by the Royal Netherlands Meteorological Institute (KNMI). The ETH (1 km × 1 km, 5 min) dataset was used to classify the footprints into shallow, nonshallow, or dry. ETH is based on a composite of the two C-band radars retrieved from 15 vertical elevation scans (ranging from 0.3° to 25.0°). ETH is defined as the maximum height where a predefined reflectivity threshold is exceeded. The KNMI uses a low detection threshold of 7 dBZ that, together with residual clutter, might result in unrealistically low (i.e., too close to the surface) or high ETH. Consequently, individual extremely low (below 0.5 km) and high (above 16 km) ETH pixels or those associated with precipitation intensities below 0.1 mm h^{-1} were removed before further analysis. To assess the model's sensitivity to these thresholds, two thresholds for both precipitation intensity (0.075 and 0.1 mm h^{-1}) and ETH (0.5 or 1 km) were tested. More information about the ETH product and its quality can be found in Holleman (2008) and Aberson (2011).

The same radars combined with gauges served as an indication for the precipitation intensity (1 km × 1 km, 5 min). These measurements were only used to filter marginal cases as mentioned in the previous paragraph and to investigate the relation between precipitation intensity and misclassified footprints. A summary of the dataset can be found in Bogerd et al. (2021), while more detailed information is available in Overeem et al. (2009a,b, 2011).

c. *Spatiotemporal matching and classification procedure*

The ground-based ETH dataset was used to classify the data while both the GMI Tb values and the 2D-DPR variables were used as feature data. The DPR, KNMI, and ERA5 datasets were matched with the GMI's resolution at 89 GHz. Each GMI footprint was matched to the closest ERA5 grid box or DPR footprint. The ETH observations (1 km × 1 km) that exceeded the thresholds defined in section 2b(3) were averaged using Gaussian weights over the 89-GHz-channel footprint dimensions (along-scan 4.4 km and along-track 7.2 km). The effect of sampling ETH values over various footprint dimensions using different weights is evaluated in Bogerd et al. (2024).

The averaged value is used to classify a footprint as dry (rainfall < 0.1 mm h^{-1}), shallow (ETH ≤ 3 km), or nonshallow (ETH > 3 km). This implies not all native ETH pixels within a GMI footprint necessarily have the same classification, which is especially the case for convective events. For instance, a convective event that only covers 35% of the total footprint would still be included if the averaged amount of rainfall exceeds the 0.1 mm h^{-1} threshold. The sensitivity of the model to the percentage of pixels that exceeded the threshold at their native resolution was also assessed.

d. *Random forest*

An RF ensemble scheme was used to classify the microwave radiometer observations. The RF model employs multiple decision trees during training and merges their predictions through bootstrapping and majority voting, thereby addressing individual trees' limitations (such as overfitting) and increasing the robustness of the results (Breiman 2001; Segal 2004; Hastie et al. 2009). The use of decision trees results in a relatively interpretable classification procedure, which generates the possibility of understanding why a footprint is allocated to a certain class. Furthermore, the RF model can

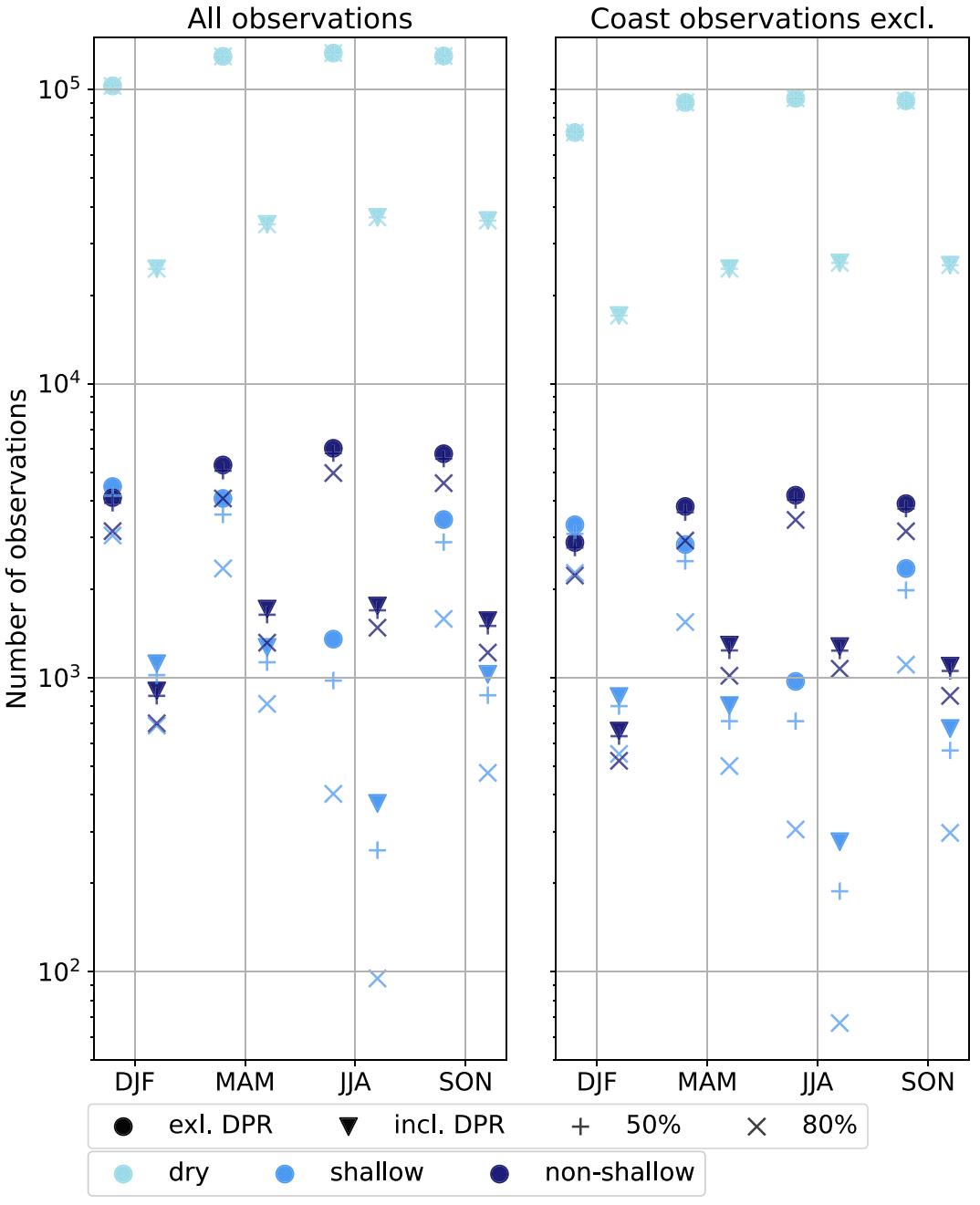

FIG. 1. The number of observations including (triangles) or excluding (circles) DPR observations. The *y* axis is logarithmic. The colors indicate the classification according to the majority of the individual reference pixels within a footprint (dry, shallow, and nonshallow). Changing the threshold from the majority of native pixels to either 50% (plusses) or 80% (crosses) reduces the number of observations. The left panel considers all observations, while the right panel excludes those located within 20 km of the coast. The markers on the left of the vertical lines refer to the number of observations when including only GMI, while the markers on the right correspond to the number of observations when the DPR is included as well.

retrieve the importance of each feature for the final decision, referred to as "permutation importance."

The permutation importance is calculated by randomly perturbing one feature and calculating its impact on the model's performance. The higher the score of a feature, the higher the model's dependency on this feature. However, these outcomes are only representative of the evaluated RF model. Additionally, correlated features may receive low scores as the model can access them through each other (Gregorutti et al. 2017). Therefore, the permutation importance is only used as an

indication. More information about the RF model and its implementation in weather-related studies can be found in the aforementioned references and Biau and Scornet (2016), Herman and Schumacher (2018), and Wolfensberger et al. (2021).

1) MODEL SETTINGS

This section elaborates on the training and validation procedure of the RF model, based on five years of data (2016–20). The results discussed in section 3 are based on the independent test data (2015 and 2021).

The RandomizedSearchCV from scikit-learn (Pedregosa et al. 2011) was used to find the best values of the following four hyperparameters: number of decision trees, maximum depth of each tree, minimal number of samples required to split a node ("decision point"), and minimum number of samples required to create a "leaf" node (final node determining the classification). Instead of examining all combinations, RandomizedSearchCV randomly samples hyperparameter combinations within a specified range to advance the tuning process. The training data are split into multiple subsets during the cross-validation. Subsequently, the RF model is trained (training) with a set of hyperparameters on one data subset, while its performance is evaluated (validated) on another subset.

The choice of parameter settings had a smaller impact on the performance than other choices. These choices involved: coast inclusion, exclusion of single lower-frequency channels (<85 GHz), percentage of ETH observations at their native resolution that could deviate from the footprint classification (section 2c), inclusion of ancillary information (DPR and/or ERA5), and combinations of these choices. All models were optimized using RandomizedSearchCV. The abbreviation of the models as used in this manuscript and the input features are specified in Table 1.

The Netherlands experiences rainfall on average 7% of the time, with approximately 93% of the studied footprints being dry according to the reference dataset (not shown). As a consequence, the dataset is highly imbalanced when considering the three targeted classes (dry, shallow, and nonshallow). To prevent any category occurrence bias, the model is trained on a balanced dataset. The number of dry observations was reduced to match the number of the shallow category using random sampling. The test dataset was also balanced to give a more accurate overview of the model performance. However, data will be imbalanced in operational applications. Hence, the model is also tested on an imbalanced dataset (i.e., using all observations of 2015 and 2021) to show how balancing affects the model's score, referred to as IM-BASIC (Table 1).

As mentioned in section 2a(1), the seasonal cycle influences precipitation characteristics (also shown in Fig. 1). Additionally, the seasonal cycle can affect both background radiation and characteristics, such as temperature differences between land and sea. Consequently, the model was trained and tested on seasonal datasets (winter: DJF; spring: MAM; summer: JJA; and fall: SON).

Figure 1 shows the number of observations within each class for the (imbalanced) test dataset using different input features and seasons. As expected, the summer season has the lowest occurrence of shallow precipitation, while the occurrence is highest in winter. Furthermore, Fig. 1 indicates the number of observations remaining after: 1) excluding the coast, 2) including DPR observations (smaller swath compared to GMI), and 3) increasing the threshold for classifying a certain footprint as shallow, nonshallow, or dry from majority to 50% (thin pluses) or 80% (crosses) of valid native ETH pixels (section 2c; footprints not exceeding the majority threshold are not included in further analysis).

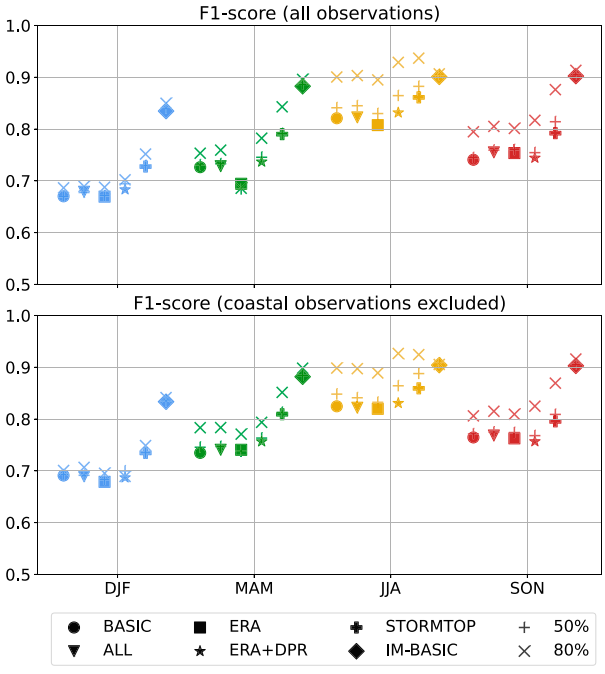

FIG. 2. The F1 scores for the RF model grouped by input features as specified in Table 1. The colors represent the different seasons. The upper panel considers all observations over land, and the lower panel considers only those at least 20 km from the coast. Similar to Fig. 1, the effect of changing the threshold from the majority of native pixels to either 50% (plusses) or 80% (crosses) is also included.

2) MODEL EVALUATION

While accuracy is a common metric to assess machine learning models, it is more suitable for balanced datasets. As an imbalanced test dataset was included as well (IM-BASIC), all models were evaluated using the less intuitive F1 score, which is suitable for both balanced and imbalanced datasets. The F1 score is defined as

$$\text{F1 score} = \frac{2 \times \text{precision} \times \text{recall}}{\text{precision} + \text{recall}}, \tag{1}$$

with precision defined as

$$\text{precision} = \frac{\text{true positives}}{\text{true positives} + \text{false positives}}, \tag{2}$$

and recall (also called sensitivity) as

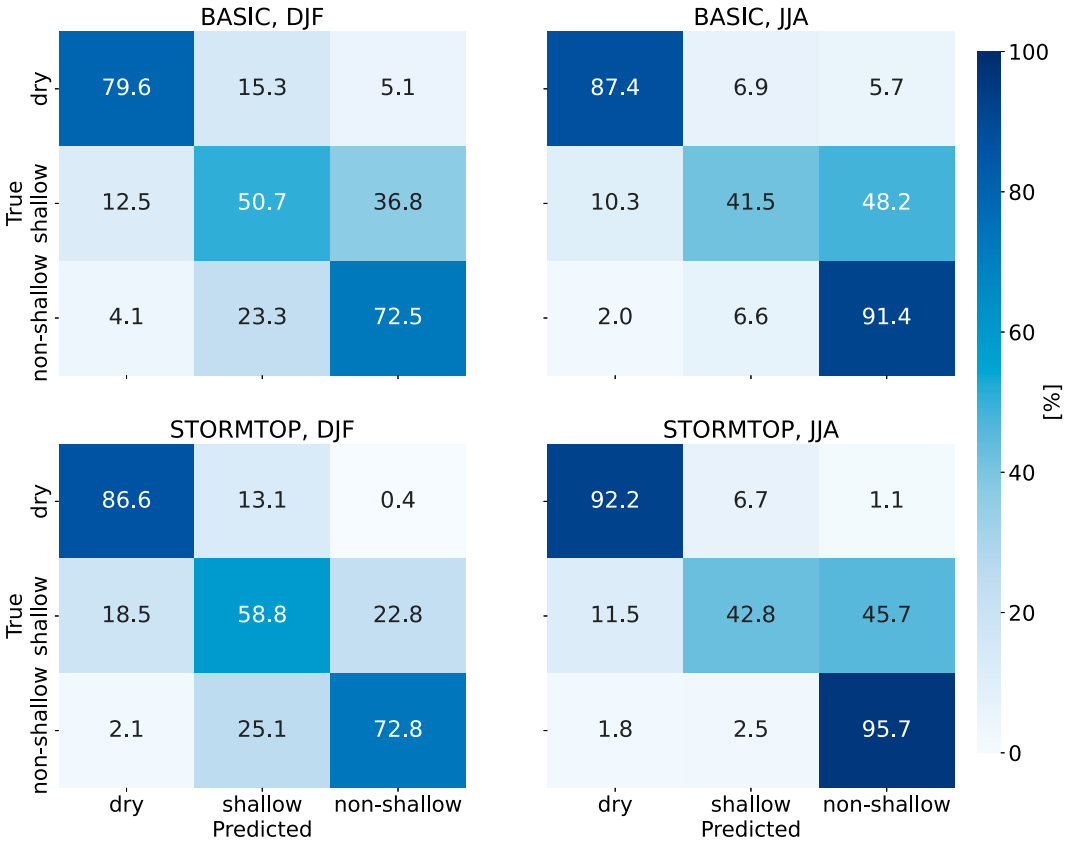

FIG. 3. The confusion matrices for (left) winter and (right) summer for (top) BASIC and (bottom) STORMTOP. The *x* axis shows the predicted class according to the RF model; the *y* axis shows the class according to the reference. Hence, the diagonal from the top left to the bottom right shows the correctly classified footprints. Each row adds up to 100%, i.e., the percentage indicates how many footprints of class 1 are classified correctly, wrongly as class 2, and wrongly as class 3. Note that the lower panel is based on a reduced number of observations (Fig. 1).

$$\text{recall} = \frac{\text{true positives}}{\text{true positives} + \text{false negatives}}. \quad (3)$$

The F1 score varies between 0 and 1, where 1 indicates the model is perfect.

Furthermore, confusion matrices were used to assess the model. A confusion matrix presents the model predictions by sorting them into categories, such as true positives or true negatives, and is closely related to precision and recall. Hence, a confusion matrix gives insight into the model's performance per class (dry, shallow, and nonshallow), resulting in a 3 × 3 matrix for this study.

In addition to these evaluations, which all focus on the RF model, the characteristics of the classified footprints were analyzed. Three groups were generated: correctly classified footprints, footprints misclassified as class 1, and footprints misclassified as class 2. For instance, if the correct class is "dry," class 1 would be "shallow," and class 2 would be

TABLE 2. Most important input features according to the permutation importance, distinguished by season and input of the RF model (as defined in Table 1). "Minimal differences" are mentioned when the highest permutation importance is below 0.025. 166V − 23V GHz represents subtracting 23.7V observations from 166V observations; 183 ± 7− 23 GHz represents subtracting 23.7V observations from 183 ± 7 observations. Note that the ALL and BASIC models have the same important parameters. The last row represents the model trained and tested on all seasons.

	BASIC and ALL	ERA	ERA + DPR	STORMTOP
DJF	183 ± 7, 166V − 23V	183 ± 7, 89V-H (166V − 23V excl. coast)	Minimal differences	heightStormTop
MAM	166V − 23V, 183 ± 7	183 ± 7, 166V − 23V (166H excl. coast)	166V, 166H	heightStormTop, 166V
JJA	166V − 23V, 166H	166H, 166V − 23V	Minimal differences	heightStormTop
SON	166V − 23V, 183 ± 7	166V, 166H (166V − 23V excl. coast)	166V, heightBB	heightStormTop
All seas	166V − 23V, 183 ± 7–23	166V − 23V, T2M (166H excl. coast)	Minimal differences	heightStormTop

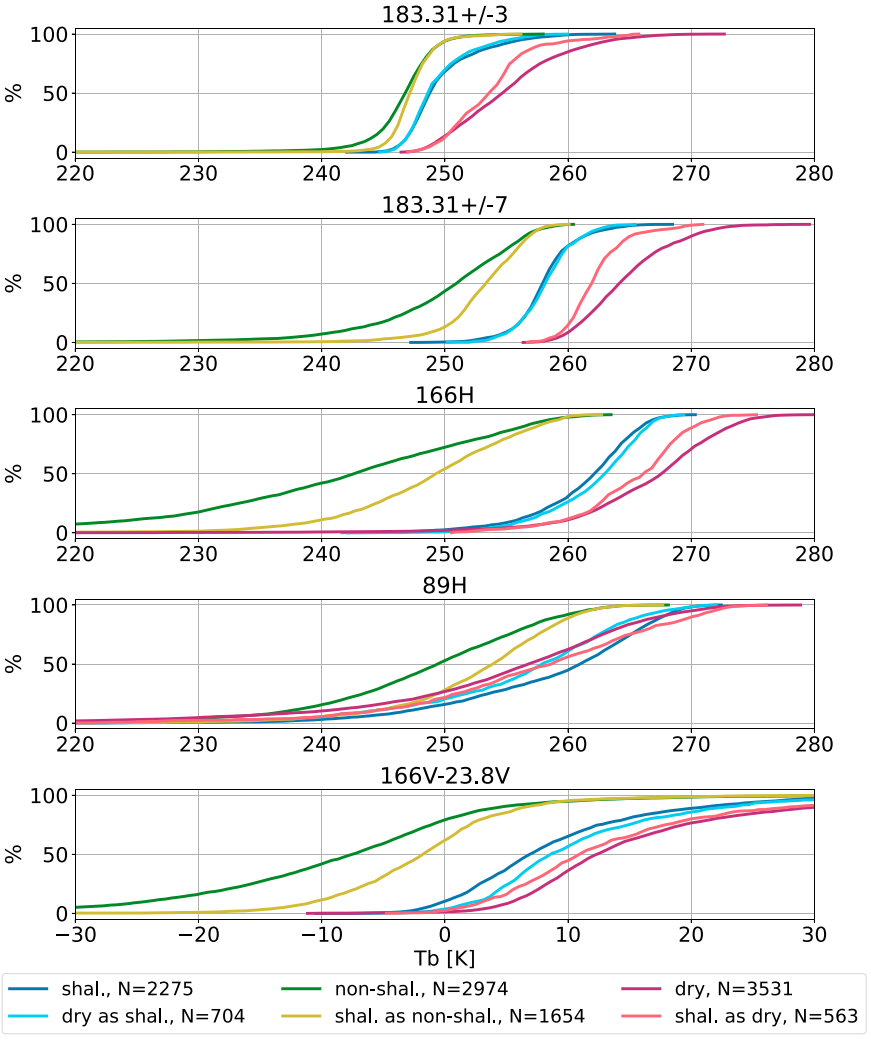

FIG. 4. CDFs of the Tb observed by the high-frequency channels. Note that not all were marked as important according to the permutation importance (Table 2). Each panel represents one channel, except for the bottom panel, which shows 166V − 23V GHz values that were often marked as important. The darker colors represent the true and correctly classified footprints (blue shallow, green nonshallow, and purple dry). The lighter colors represent the wrongly classified footprints (light-blue is dry classified as shallow, light-green is shallow classified as nonshallow, and salmon is shallow classified as dry). Only the winter season is considered. The classification is retrieved using BASIC.

"nonshallow." Cumulative distribution functions (CDFs) and the 25th, 50th, and 75th percentiles were used to identify the characteristics of each group. Furthermore, three overpasses were examined as case studies, to unravel the performance of the model.

3. Results

The F1 score (Fig. 2) is lowest during winter (between 0.65 and 0.82) and highest during summer (between 0.81 and 0.95). Excluding the coast (lower panel) only slightly increases the F1 score. Testing on an imbalanced dataset [section 2d(2)] increases the performance in all seasons, with the smallest increase in summer. The increased F1 score when the test dataset is imbalanced is most likely related to the correct classification of the majority class, which are dry footprints. Increasing the threshold to 80% (crosses) of the native pixels that should belong to one class improves the F1 score, as those cases fill (almost) the entire footprint and are associated with stronger radiometric signals. This increase in threshold increases the performance of the model in all seasons, with the most notable improvements in summer and the smallest in winter. However, note that the number of observations is limited, especially during summer (Fig. 1). The scores for BASIC, ALL, and ERA, are comparable, except for ERA during spring over the entire land surface (upper panel). This indicates that the

addition of the single low frequencies and ERA parameters has a limited positive impact. Including all 2D-DPR variables (thick plusses) improves the model during all seasons, but this effect is reduced when excluding the stormtopheight parameter (stars).

The confusion matrices provide insight into the model's performance per class (Fig. 3). The upper panel of Fig. 3 shows the matrices using BASIC input features, and the lower panel of Fig. 3 shows the matrices using STORMTOP. Distinguishing between dry and shallow is more difficult in winter (left panels) compared to summer (right panels). In summer, however, almost half of the shallow footprints are misclassified as nonshallow (upper-right panel). Including ERA5 and DPR improves the correct classification of dry and shallow in winter from 50.7% to 58.8% but only slightly improves the correct detection of nonshallow footprints in both seasons (0.8% in winter and 4.3% in summer) and shallow in summer (1.3%). Furthermore, including the STORMTOP increases the "misses" of shallow observations (lower panel), especially in winter.

The results of the permutation importance [section 2d(2)] are summarized in Table 2. The scores remained 0.11 or lower, suggesting limited dependency on individual input features likely caused by cross correlation between the input features. In general, the 166-GHz channel (either horizontal, vertical, or in relation to a lower-frequency channel) is found to be important. The polarization difference between the 89-GHz channels is prominent in winter; the polarization difference between the 166V − 23V GHz channels is prominent during all seasons; and the polarization difference between the 183 ± 7 GHz channels is prominent in spring, winter, and one time in fall. Excluding the storm top (ERA + DPR) shows the importance of the other 2D-DPR products is limited, as the differences are either minimal or Tb channels are the most important, except for fall (heightBB).

Figures 4–6 focus on winter, the season with the most frequent shallow precipitation (Fig. 1), and aim to identify shared characteristics among the three classes. The top four panels of Fig. 4 illustrate the Tb distribution obtained from individual high-frequency channels (the other seasons are shown in Figs. S1–S3 in the online supplemental material). The bottom panel shows the combination of a high-frequency channel (166V, representing the interaction with precipitation particles) and a low-frequency channel (23.8V, representing the background emissions). Although the value range of the three classes often overlaps, nonshallow footprints are typically characterized by lower Tb values, dry footprints by higher Tb values, and shallow in between. This result is expected, as ice decreases Tb values observed by higher-frequency channels and nonshallow precipitation is associated with more ice than shallow precipitation. The distributions of accurately classified footprints and those that are misclassified to the same class are similar, especially in the upper three rows. For instance, the distribution of Tb associated with dry footprints classified as shallow is similar to the distribution of "true" shallow footprints.

The distributions of the reference data are shown (Fig. 5) to analyze whether the misclassified observations are associated with values near the boundary of two classes. Precipitation intensity and ETH of footprints wrongly classified as nonshallow (dry) are higher (slightly lower) compared to those correctly classified as shallow.

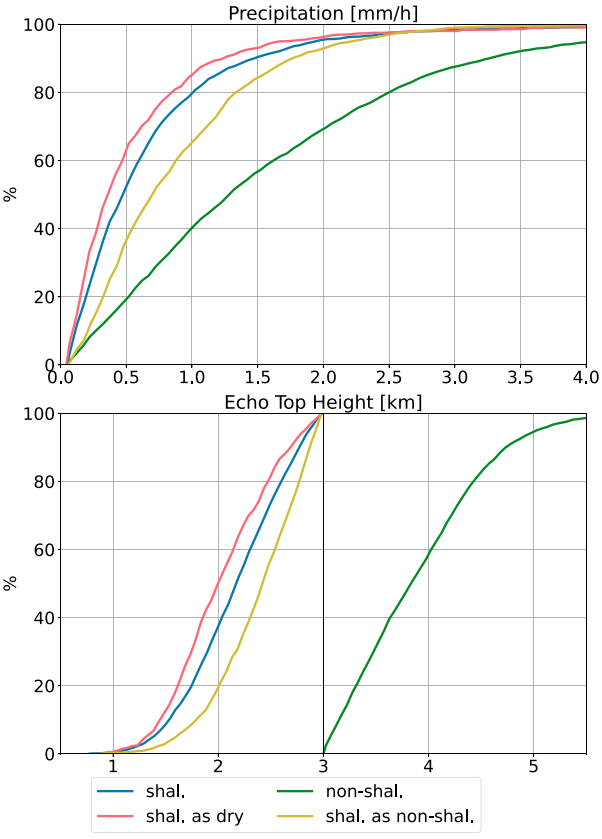

FIG. 5. CDFs of the (top) precipitation intensity and (bottom) ETH in winter. The settings are similar to Fig. 4. Note that this information is not provided to the RF model as it involves reference characteristics. Additionally, note that only wet footprints were included.

Figure 6 shows the attenuation-corrected vertical profiles retrieved from the DPR associated with GMI footprints. The higher sensitivity of the Ka band makes it more susceptible to attenuation, reducing the number of valid observations (the number of observations is shown in the legend). The reflectivity values of the nonshallow events in winter are higher than those associated with shallow footprints (both correctly and most of the incorrectly classified). Shallow footprints wrongly classified as dry were not detected by the DPR, indicating a weak reflectivity signal observed by spaceborne sensors. These results are in agreement with those shown in Fig. 4: adding DPR observations does not increase the RF's capability to detect shallow precipitation wrongly classified as dry. Additionally, less than half of the shallow footprints are captured by the Ku band, and only a third of them are captured by the Ka band, indicating that shallow events are often missed by the DPR.

Shallow footprints classified as dry are associated with relatively high Tb values (Fig. 4) and are not detected by the DPR (Fig. 5), indicating weak signatures or associated cloud

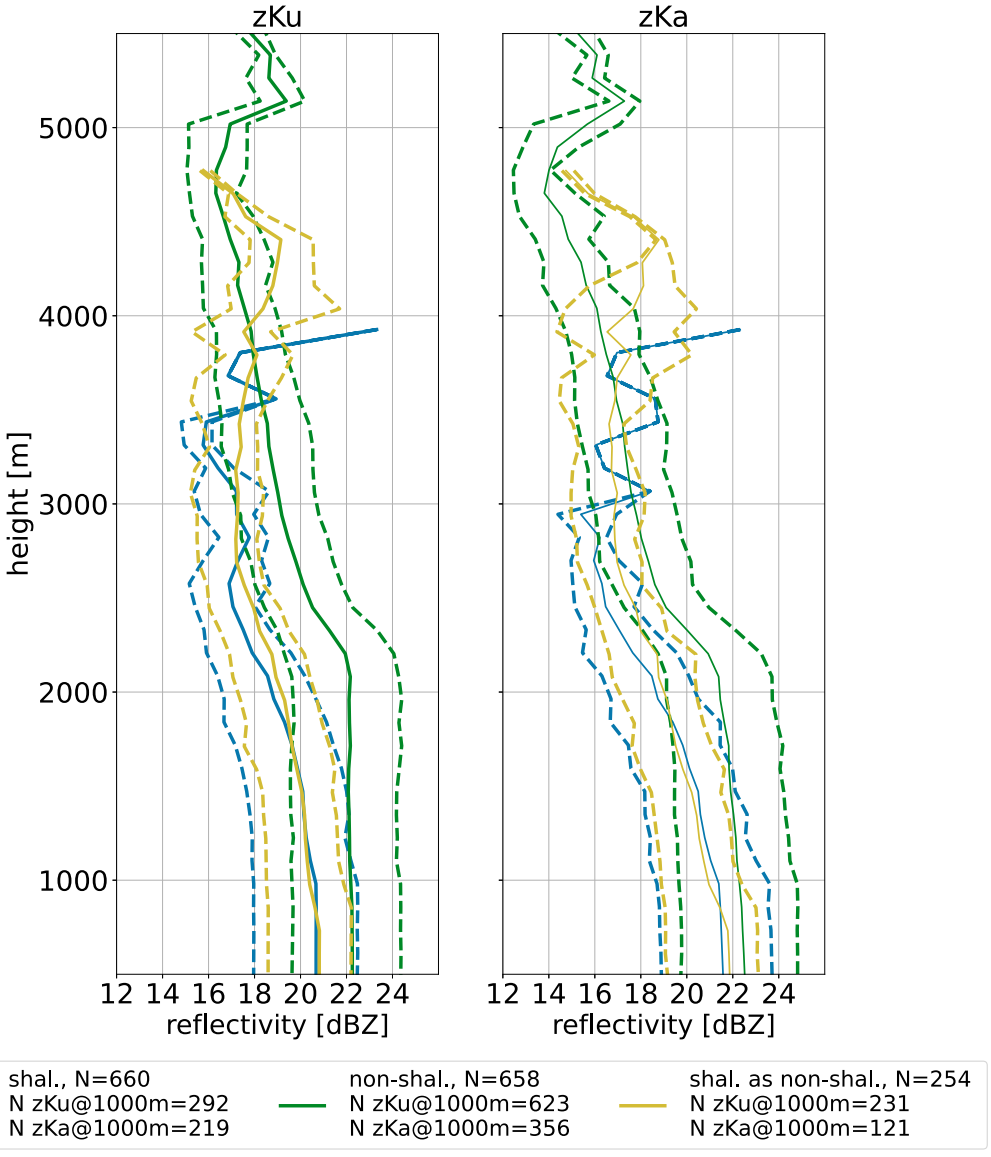

FIG. 6. The 25th and 75th percentiles (dashed) and mean (solid) of the vertical reflectivity profiles corresponding to GMI footprints in winter. The horizontally polarized radar reflectivity factor values are retrieved from matched DPR observations. The number of observations retrieved by the Ka band is lower than those retrieved from the Ku band. The number of observations above 3000 m for shallow footprints wrongly classified as nonshallow is limited. The classification was retrieved using STORMTOP. Note that this information is not provided to the RF model.

height is below 1 km (or 1.5 km at the edges of the DPR swath). Conversely, dry footprints misclassified as shallow are associated with lower Tb values. Two cases are selected to further unravel why those footprints are allocated to another class.

Case studies are used to gain some additional insight. The first case (Fig. 7) is relatively well classified although dry footprints at the precipitation system border are wrongly labeled as shallow. Footprints associated with nonshallow precipitation correspond to relatively low Tb values observed by the 166H and 183.31 ± 7 GHz (especially at the northern and western edges) channels compared to the Tb values associated with correctly classified dry footprints. As shown in Fig. 4, observations associated with Tb values in between nonshallow and dry are classified as shallow. "Dry footprints" that are incorrectly classified as shallow show values similar to those correctly classified as shallow, especially at the northern and southern edges of the precipitation system.

As previously explained, precipitating clouds are often associated with ice particles, which lower the Tb values measured at higher frequencies. However, ice could also be present in nonprecipitating clouds. Geostationary satellite observations from Meteosat Second Generation (MSG)-SEVIRI (third panel, Fig. 7) indeed suggest the presence of ice particles over the Netherlands, except north of 53°N where the RF model

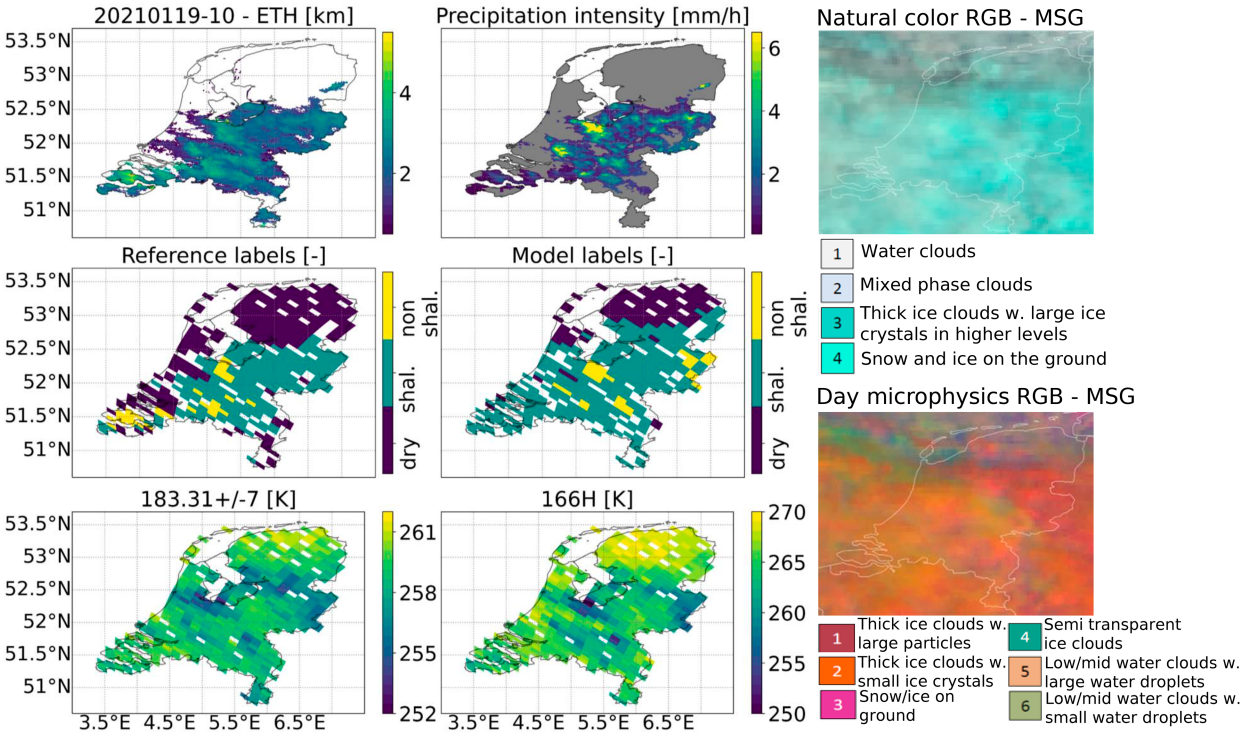

FIG. 7. Case study 1: 19 Jan 2021. The left two upper panels show the reference values at the native resolution (1 km × 1 km); the two left middle panels show the classification according to the reference (left) or the RF model (middle); and the two lower-left panels show the Tb values for two of GMI's high-frequency channels. Footprints are not classified if the reference precipitation and ETH observations did not exceed the thresholds as defined in section 2c or if one of the GMI frequency channels lacked observations. The right panel shows two images of the geostationary MSG-SEVIRI satellite, which are provided by EUMETView (EUMETRAIN 2024c). The upper-right panel makes use of three solar channels: NIR1.6, VIS0.8, and VIS0.6. The lower-right panel shows the results of the microphysics algorithm based on three channels: VIS0.8, IR3.9, and IR10.8.

correctly classified the observations as dry. The presence of ice is indicated by the cyan color in the data obtained from channels associated with the visible spectrum (upper-right panel, Fig. 7) and by the reddish color indicated by the microphysics algorithm (middle-right panel, Fig. 7). More information about the two algorithms can be found at EUMETRAIN (2024b,d) and references therein.

The second case involves an overpass almost completely classified as shallow instead of dry (middle panels, Fig. 8). Similar to the previous case, the values observed by the two high-frequency channels are in the value range associated with shallow precipitation (Fig. 4). In agreement with the previous case, clouds with ice particles are present according to the MSG-SEVIRI observations (right panels, Fig. 8).

A third case study involves a narrow band of shallow precipitation with a limited scattering signal (lower panel, Fig. 9). Right of the IJsselmeer (approximately 42.5°N, 6.0°E), the narrow band of shallow precipitation is only partly classified correctly, while left of the IJsselmeer (approximately 42.75°N, 5.75°E), the footprints are classified as dry. Both algorithms based on the MSG-SEVIRI data indicate the presence of mixed-phase clouds (upper-right panel, Fig. 9), which might confuse the algorithm as a result of a limited decrease in Tb values (lower panel, Fig. 9).

4. Discussion

This study is the first to classify microwave radiometer observations as dry, shallow, or nonshallow using a random forest model over such a northern location. We tested the model's sensitivity to input features and the implemented thresholds on the reference data. Adjusting the thresholds, as specified in section 2b(3), only slightly affected the F1 scores (maximum ± 0.1), independent of the input features, and did not significantly affect the important features according to the permutation difference (not shown). Although other models might yield better results, such as a neural network, the RF model was chosen for reasons given in section 1.

The GMI sensor is equipped with high-frequency channels to improve the detection of light-intensity events in comparison to its predecessor that served during the Tropical Rainfall Measuring Mission (TRMM), the TRMM Microwave Imager (TMI). As shallow precipitation over the Netherlands is often associated with light precipitation, we also hypothesized these channels to be important for the RF model. The higher-frequency channels were indeed important for the RF model, but it remained difficult to accurately separate dry and shallow events. Various explanations are discussed below.

First, the algorithm might be overly sensitive. This sensitivity is likely induced by the relatively weak scattering signal

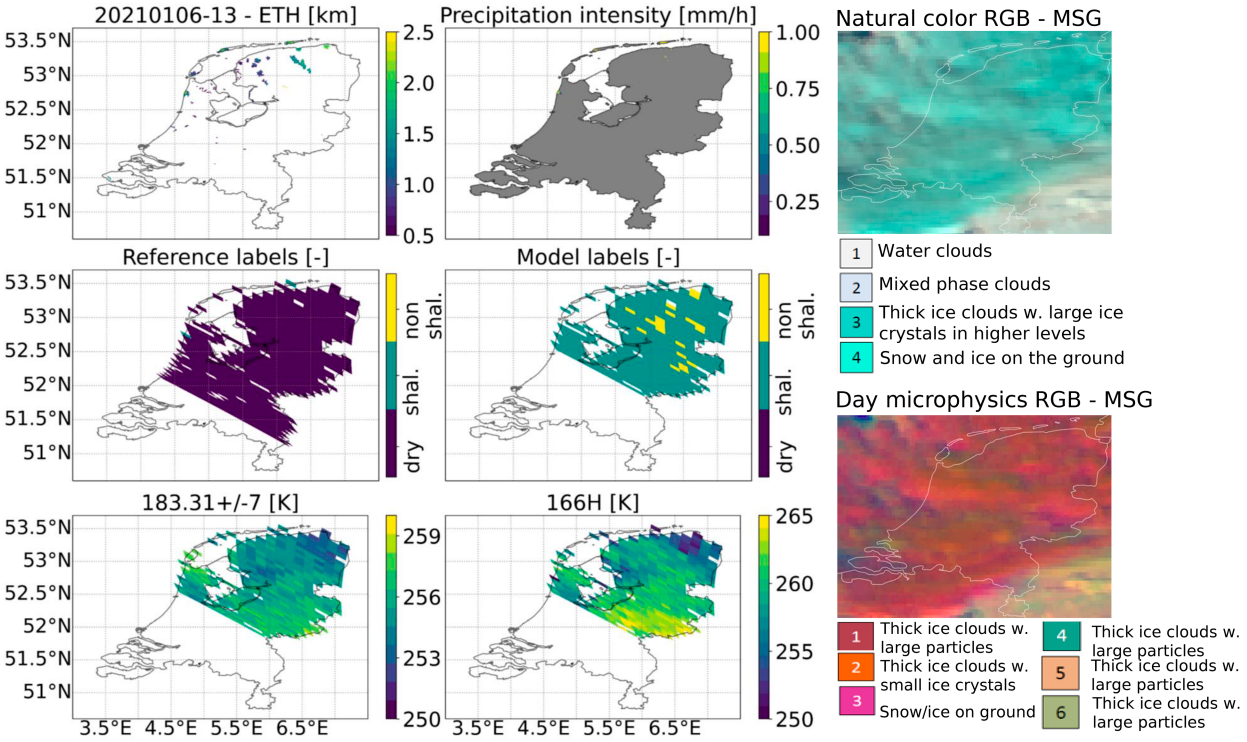

FIG. 8. Case study 2: 6 Jan 2021. Dry footprints classified as shallow. The settings are similar to Fig. 7, except for the color scale of the upper panel. The reference labels cover a larger area than the model labels due to the absence of high-frequency observations at the edges of the GMI swath.

associated with (stratiform) shallow events (Weng and Grody 2000; Kida et al. 2009, 2018). As a consequence, the random forest model learns to identify even the smallest decreases in brightness temperatures as shallow precipitation. However, as a drawback of this sensitivity, slight decreases in brightness temperatures related to nonprecipitating ice clouds, such as thick cirrus clouds or multilayered clouds, are also subjective to be classified as shallow, as shown in the two case studies (Figs. 7 and 8).

Second, as expected, the presence of ice particles seems to be a condition for the RF model to detect (shallow) precipitation. However, due to the limited vertical extent associated with shallow precipitation, the cloud top might be located below the freezing level. As a consequence, scattering related to ice particles is absent, and only the emission of liquid water can be detected (Lebsock et al. 2011). These "warm" rain processes over land surfaces are hard to distinguish from nonprecipitating clouds by spaceborne microwave radiometers (Stephens and Kummerow 2007). Another source resulting in a limited scattering signal is the presence of liquid water above the freezing level (Matrosov and Turner 2018). Both the absence of and limited scattering signal related to ice particles might result in shallow footprints being classified as dry (Fig. 9).

The difference in results with, for instance, the overview paper of Turk et al. (2021) might be related to our regional approach and focus on distinguishing dry, shallow, and nonshallow footprints instead of characterizing background surfaces. Our focus enhances the relative importance of higher-frequency channels due to the interaction with water vapor and scattering of ice particles. However, including observations from low-frequency channels through subtraction from high-frequency channels demonstrated a slightly higher F1 score, ranging from 0.1 to 0.3 higher depending on the season, compared to when low frequencies were included separately (not shown).

Another hypothesis that has been discussed is the possibility that lower Tb values are the product of wet surface conditions, which the RF model misinterprets as colder clouds. We found consistently lower Tb values measured by the 18.7-GHz channel over water-saturated areas such as rivers and low-laying land (not shown). However, these areas did not overlap with the locations of dry footprints wrongly classified as shallow. Additionally, higher-frequency channels did not observe lower values over these areas (Figs. 7 and 8, lower panels). Furthermore, the sky was often cloudy when dry footprints were classified as shallow (Figs. 7 and 8, right panels). In general, our algorithm seems less affected by background radiation due to the limited importance of lower-frequency channels. This limited role of the lower-frequency channels and the relatively small footprint size of the GMI could also explain the limited influence of the coast, which contrasts with the results of previous research (Bennartz 1999; Munchak and Skofronick-Jackson 2013).

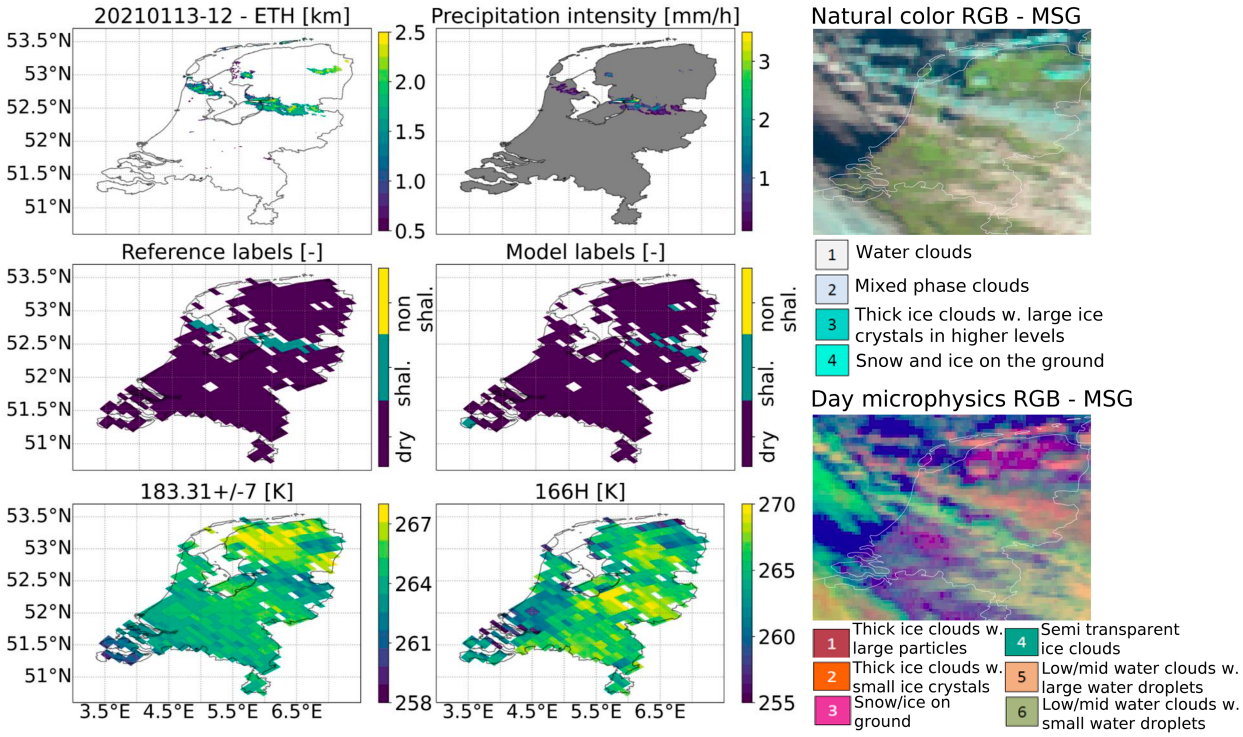

FIG. 9. Case study 3: 13 Jan 2021. A narrow precipitation event that is partly correctly detected and partly missed (left of the IJsselmeer). The settings are similar to Fig. 8, except for the color scale of the upper panel.

Unfortunately, at least three cases with numerous shallow footprints classified as dry occurred during nighttime when geostationary VIS observations are unavailable. Although algorithms solely based on IR observations can also deduce cloud-phase information, their accuracy is lower than those including VIS observations (Costa et al. 2007; Iwabuchi et al. 2016; Escrig et al. 2013). Additionally, interpreting IR images is more complex than those based on IR/VIS observations and is considered out of scope for the current analysis. We also explored matched observations with Advanced Technology Microwave Sounder (ATMS), SSMIS, and Time-Resolved Observations of Precipitation structure and storm Intensity with a Constellation of Smallsats (TROPICS) (radiometers equipped with higher-frequency channels), but the number of matched footprints with GMI was limited.

The performance of geostationary cloud-phase retrieval algorithms that combine IR/VIS observations is only qualitative and may not work well over snow-covered surfaces or low solar zenith angles (Lensky and Rosenfeld 2008; EUMETRAIN 2024a), but the impact of these limitations is expected to be limited as there was no snow cover during the considered case studies. Since the areas flagged as (thick) ice clouds by both algorithms considered in this study appear to correlate well with errors in the RF algorithm (Figs. 7 and 8, right panels), it seems beneficial to include the geostationary satellites to separate between dry, shallow, and nonshallow footprints.

The authors are aware that the spatial coverage of the current study could be extended globally if DPR observations were used as a reference. However, as mentioned in section 1 and confirmed in the results of this study (section 3), the performance of DPR regarding shallow precipitation is limited. This result again amplifies the need for reliable calibration and validation data. At the same time, our results suggest that DPR observations could improve the classification between shallow and nonshallow precipitation systems.

The frequent occurrence of convective events in summer results in an overrepresentation of nonshallow footprints (Fig. 3). This overrepresentation is reduced when using the ALL model (Fig. 10). Although this improves the classification between dry and rainy footprints (i.e., shallow and nonshallow) in summer, the ALL model showed a decreased performance in classifying dry and rainy footprints in winter when most shallow events occur.

The F1 scores corresponding to the ALL model distinguished by season and various input parameters are shown in Fig. 11. Compared to the seasonal models (Fig. 2), the F1 scores of the ALL, BASIC, and ERA models decreased for all seasons (Fig. 11). These results again confirm the limited importance of ERA parameters, even when applying a more general model in the time aspect. In contrast, Fig. 11 also demonstrates the added value of DPR observations despite DPR's limitations in detecting shallow precipitation.

The limited importance of ERA5 parameters, which is contrary to findings in prior studies, is attributed to the regional focus. Seasons implicitly provide environmental information, for instance, due to the clustering of temperature. Table 2 demonstrates that ERA5 temperature is more important when

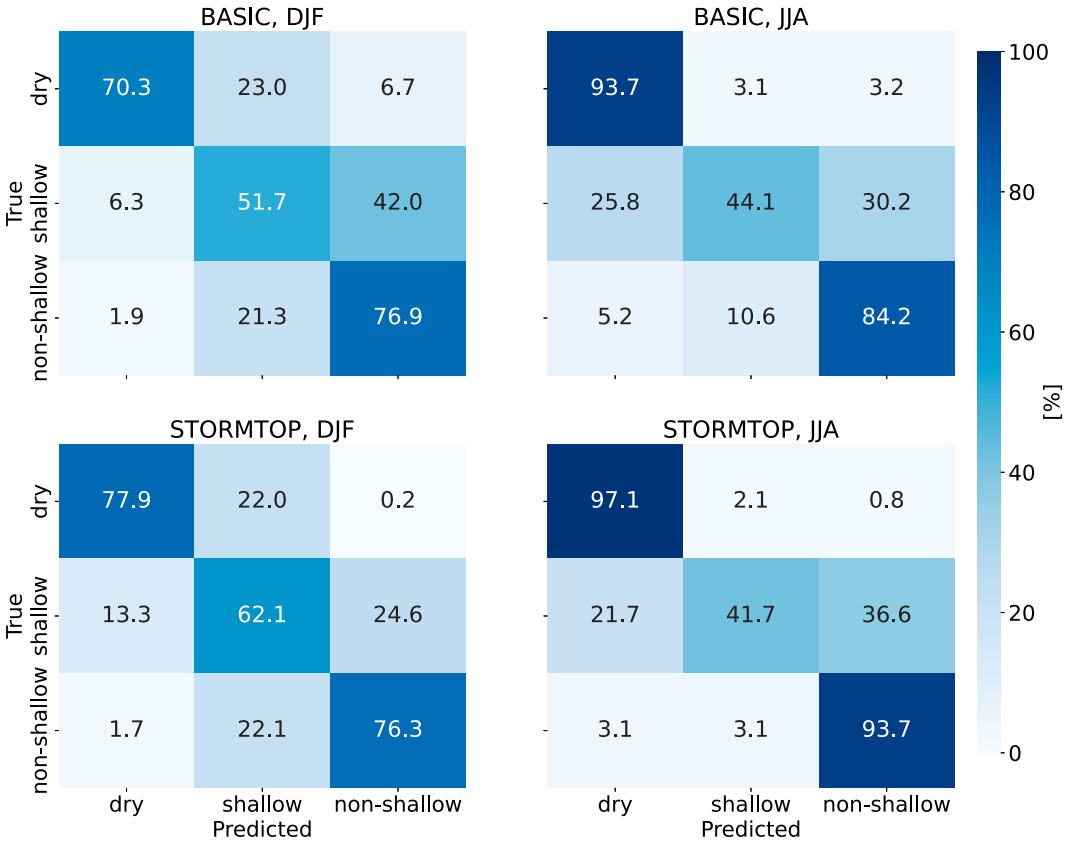

FIG. 10. As in Fig. 3, but applying the model based on the entire year on (left) DJF and (right) JJA. The upper panel does not include the DPR; the lower panel includes the DPR. The tested dataset was balanced.

training the model in all seasons. Additionally, we included ERA5 moisture data to mitigate the impact of varying moisture levels (above the cloud top) on Tb values retrieved from higher-frequency channels. However, we found a limited impact of atmospheric moisture on the model's performance, likely due to relatively modest moisture levels over the Netherlands.

More accurate input could in principle be retrieved using 3D data. However, this study aimed to find more general relations through the use of a longer period. The amount of data when considering 3D observations would be prohibitive over such a time frame. Instead, we would aim to study 3D radar fields (i.e., coupling microwave radiometer observations to ground-based radars) in relation to case studies, preferably from a vertically pointing rain radar, to unravel the vertical structure of the atmosphere and to confirm our earlier hypotheses related to the presence/absence of ice particles.

Sections 3 and 4 both focus on the wrongly classified shallow and dry footprints, while only little attention is paid to the nonshallow footprints. As previously stated, this study aims to improve the detection of (shallow) precipitation with radiometers. Nonshallow precipitation is almost always detected: even if wrongly classified, nonshallow footprints are almost never classified as dry (Figs. 3 and 10). The reason to still include the separation between shallow and nonshallow was to point out that missed precipitation mostly involved shallow precipitation.

5. Conclusions

The retrieval of light and/or shallow precipitation estimates from spaceborne microwave radiometer observations is challenging, especially over land. This study implemented a random forest (RF) model that used microwave radiometer observations from the Global Precipitation Measurement (GPM) mission as input to distinguish dry, shallow, and nonshallow footprints over a high-latitude region. The RF model, trained on five years of data and tested on two independent years, performed worst in winter (F1 score ranging from 0.68 to 0.75) and best in summer (F1 score ranging from 0.81 to 0.92), independent of the input features. The model had difficulties distinguishing shallow and nonshallow in both seasons, but more in summer (48.2% of the shallow events classified as nonshallow) than in winter (36.8%). In contrast, distinguishing between shallow and dry footprints was more challenging in winter when 12.5% of shallow footprints were wrongly classified as dry and 15.3% of the dry footprints were wrongly classified as shallow. Shallow footprints associated with a limited scattering signal were wrongly classified as dry, while dry footprints associated with relatively low brightness temperatures observed by higher-frequency channels (≥85 GHz) were wrongly classified as shallow.

This study confirmed the importance of high-frequency channels for spaceborne precipitation retrieval over land, while at the same time, the added value, when combining these

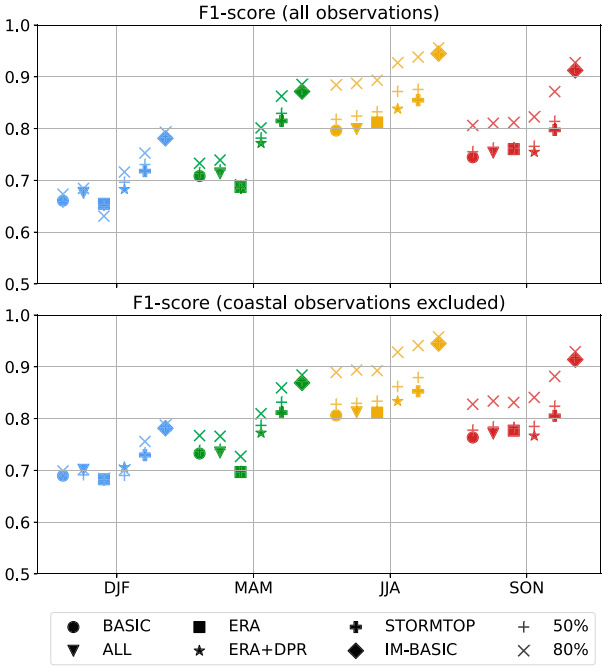

FIG. 11. As in Fig. 2, but applying the model based on the entire year on the four different seasons.

observations with those retrieved from low-frequency channels, was demonstrated. Furthermore, the implementation of the RF model and analysis of the wrongly identified footprints improved our understanding of the difficulties associated with distinguishing between shallow and dry footprints in a moderate maritime climate. This method could be extended to other regions as well to further unravel the difficulties associated with precipitation retrieval from spaceborne microwave radiometers. This study also indicated the potential to improve spaceborne precipitation detection by merging observations retrieved from both geostationary and low-Earth-orbiting satellites. For future studies concerning spaceborne precipitation retrieval over northern latitudes, we recommend using vertically pointing radars to study the microphysics associated with shallow events.

Acknowledgments. We acknowledge financial support from the Dutch Research Council (NWO) through project ALWGO.2018.048. Additionally, we thank Giulia Panegrossi and Lisa Milani for their valuable contributions and ideas on shallow precipitation. Furthermore, we highly appreciate the input of Mircea Grecu regarding the GPM–DPR instrument. We also thank the two anonymous reviewers for their constructive comments and suggestions.

Data availability statement. GPM data can be retrieved from https://gpm.nasa.gov/data/directory. MSG data can be retrieved from https://data.eumetsat.int/search?query=. KNMI ETH data can be retrieved from https://dataplatform.knmi.nl/dataset/radar-tar-echotopheight-5min-1-0. KNMI precipitation data can be retrieved from https://dataplatform.knmi.nl/dataset/rad-nl25-rac-mfbs-5min-netcdf4-2-0.

REFERENCES

Aberson, K., 2011: The spatial and temporal variability of the vertical dimension of rainstorms and their relation with precipitation intensity. KNMI Internal Rep. IR 2011-03, 44 pp.

Adhikari, A., and A. Behrangi, 2022: Assessment of satellite precipitation products in relation with orographic enhancement over the western United States. *Earth Space Sci.*, **9**, e2021EA001906, https://doi.org/10.1029/2021EA001906.

——, C. Liu, and L. Hayden, 2019: Uncertainties of GPM microwave imager precipitation estimates related to precipitation system size and intensity. *J. Hydrometeor.*, **20**, 1907–1923, https://doi.org/10.1175/JHM-D-19-0038.1.

Anagnostou, E. N., 2004: Overview of overland satellite rainfall estimation for hydro-meteorological applications. *Surv. Geophys.*, **25**, 511–537, https://doi.org/10.1007/s10712-004-5724-6.

Arulraj, M., and A. P. Barros, 2017: Shallow precipitation detection and classification using multifrequency radar observations and model simulations. *J. Atmos. Oceanic Technol.*, **34**, 1963–1983, https://doi.org/10.1175/JTECH-D-17-0060.1.

Awaka, J., M. Le, V. Chandrasekar, N. Yoshida, T. Higashiuwatoko, T. Kubota, and T. Iguchi, 2016: Rain type classification algorithm module for GPM dual-frequency precipitation radar. *J. Atmos. Oceanic Technol.*, **33**, 1887–1898, https://doi.org/10.1175/JTECH-D-16-0016.1.

Behrangi, A., K.-L. Hsu, B. Imam, S. Sorooshian, G. J. Huffman, and R. J. Kuligowski, 2009: PERSIANN-MSA: A precipitation estimation method from satellite-based multispectral analysis. *J. Hydrometeor.*, **10**, 1414–1429, https://doi.org/10.1175/2009JHM1139.1.

——, Y. Tian, B. H. Lambrigtsen, and G. L. Stephens, 2014: What does CloudSat reveal about global land precipitation detection by other spaceborne sensors? *Water Resour. Res.*, **50**, 4893–4905, https://doi.org/10.1002/2013WR014566.

Bennartz, R., 1999: On the use of SSM/I measurements in coastal regions. *J. Atmos. Oceanic Technol.*, **16**, 417–431, https://doi.org/10.1175/1520-0426(1999)016<0417:OTUOSI>2.0.CO;2.

Biau, G., and E. Scornet, 2016: A random forest guided tour. *Test*, **25**, 197–227, https://doi.org/10.1007/s11749-016-0481-7.

Bogerd, L., A. Overeem, H. Leijnse, and R. Uijlenhoet, 2021: A comprehensive five-year evaluation of IMERG late run precipitation estimates over the Netherlands. *J. Hydrometeor.*, **22**, 1855–1868, https://doi.org/10.1175/JHM-D-21-0002.1.

——, H. Leijnse, A. Overeem, and R. Uijlenhoet, 2024: Assessing sampling and retrieval errors of GPROF precipitation estimates over the Netherlands. *Atmos. Meas. Tech.*, **17**, 247–259, https://doi.org/10.5194/amt-17-247-2024.

Breiman, L., 2001: Random forests. *Mach. Learn.*, **45**, 5–32, https://doi.org/10.1023/A:1010933404324.

Casella, D., G. Panegrossi, P. Sanò, A. C. Marra, S. Dietrich, B. T. Johnson, and M. S. Kulie, 2017: Evaluation of the GPM-DPR snowfall detection capability: Comparison with CloudSat-CPR. *Atmos. Res.*, **197**, 64–75, https://doi.org/10.1016/j.atmosres.2017.06.018.

Cecil, D. J., and T. Chronis, 2018: Polarization-corrected temperatures for 10-, 19-, 37-, and 89-GHz passive microwave frequencies. *J. Appl. Meteor. Climatol.*, **57**, 2249–2265, https://doi.org/10.1175/JAMC-D-18-0022.1.

Chen, F., and X. Li, 2016: Evaluation of IMERG and TRMM 3B43 monthly precipitation products over mainland China. *Remote Sens.*, **8**, 472, https://doi.org/10.3390/rs8060472.

Costa, M. J., V. Levizzan, E. Cattani, and S. Melani, 2007: The retrieval of cloud top properties using VIS-IR channels.

Measuring Precipitation from Space, V. Levizzani, P. Bauer, and F. J. Turk, Eds., Springer, 79–95, https://doi.org/10.1007/978-1-4020-5835-6_7.

D'Adderio, L. P., D. Casella, S. Dietrich, P. Sanò, and G. Panegrossi, 2022: GPM-CO observations of Medicane Ianos: Comparative analysis of precipitation structure between development and mature phase. *Atmos. Res.*, **273**, 106174, https://doi.org/10.1016/j.atmosres.2022.106174.

Daniels, E. E., G. Lenderink, R. W. A. Hutjes, and A. A. M. Holtslag, 2014: Spatial precipitation patterns and trends in the Netherlands during 1951–2009. *Int. J. Climatol.*, **34**, 1773–1784, https://doi.org/10.1002/joc.3800.

Draper, D. W., D. A. Newell, F. J. Wentz, S. Krimchansky, and G. M. Skofronick-Jackson, 2015: The Global Precipitation Measurement (GPM) Microwave Imager (GMI): Instrument overview and early on-orbit performance. *IEEE J. Sel. Top. Appl. Earth Obs. Remote Sens.*, **8**, 3452–3462, https://doi.org/10.1109/JSTARS.2015.2403303.

Escrig, H., F. J. Batlles, J. Alonso, F. M. Baena, J. L. Bosch, I. B. Salbidegoitia, and J. I. Burgaleta, 2013: Cloud detection, classification and motion estimation using geostationary satellite imagery for cloud cover forecast. *Energy*, **55**, 853–859, https://doi.org/10.1016/j.energy.2013.01.054.

EUMETRAIN, 2024a: SEVIRI day microphysics RGB quick guide. Accessed 15 May 2024, https://user.eumetsat.int/resources/user-guides/day-microphysics-rgb-quick-guide.

——, 2024b: Day microphysics RGB - MSG - 0 degree. Accessed 15 May 2024, https://data.eumetsat.int/product/EO:EUM:DAT:MSG:DMRGB#.

——, 2024c: EUMETSAT productviewer. Accessed 15 May 2024, https://view.eumetsat.int/productviewer?v=default.

——, 2024d: Natural colour RGB - MSG - 0 degree. Accessed 15 May 2024, https://data.eumetsat.int/product/EO:EUM:DAT:MSG:NCL#.

Gregorutti, B., B. Michel, and P. Saint-Pierre, 2017: Correlation and variable importance in random forests. *Stat. Comput.*, **27**, 659–678, https://doi.org/10.1007/s11222-016-9646-1.

Hastie, T., R. Tibshirani, and J. Friedman, 2009: Random forests. *The Elements of Statistical Learning: Data Mining, Inference, and Prediction*, Springer, 587–604, https://doi.org/10.1007/978-0-387-84858-7_15.

Hayden, L., and C. Liu, 2021: Differences in the diurnal variation of precipitation estimated by spaceborne radar, passive microwave radiometer, and IMERG. *J. Geophys. Res. Atmos.*, **126**, e2020JD033020, https://doi.org/10.1029/2020JD033020.

Held, I. M., and B. J. Soden, 2006: Robust responses of the hydrological cycle to global warming. *J. Climate*, **19**, 5686–5699, https://doi.org/10.1175/JCLI3990.1.

Herman, G. R., and R. S. Schumacher, 2018: Money doesn't grow on trees, but forecasts do: Forecasting extreme precipitation with random forests. *Mon. Wea. Rev.*, **146**, 1571–1600, https://doi.org/10.1175/MWR-D-17-0250.1.

Hersbach, H., and Coauthors, 2020: The ERA5 global reanalysis. *Quart. J. Roy. Meteor. Soc.*, **146**, 1999–2049, https://doi.org/10.1002/qj.3803.

Hirose, M., S. Shige, T. Kubota, F. A. Furuzawa, H. Minda, and H. Masunaga, 2021: Refinement of surface precipitation estimates for the dual-frequency precipitation radar on the GPM core observatory using near-nadir measurements. *J. Meteor. Soc. Japan*, **99**, 1231–1252, https://doi.org/10.2151/jmsj.2021-060.

Hoffmann, L., and Coauthors, 2019: From ERA-Interim to ERA5: The considerable impact of ECMWF's next-generation reanalysis on Lagrangian transport simulations. *Atmos. Chem. Phys.*, **19**, 3097–3124, https://doi.org/10.5194/acp-19-3097-2019.

Holleman, I., 2008: Echotops for annotation on radar imagery. Tech. Rep. 299, 32 pp., https://cdn.knmi.nl/knmi/pdf/bibliotheek/knmipubTR/TR299.pdf.

Hou, A. Y., and Coauthors, 2014: The Global Precipitation Measurement mission. *Bull. Amer. Meteor. Soc.*, **95**, 701–722, https://doi.org/10.1175/BAMS-D-13-00164.1.

Huntington, T. G., 2006: Evidence for intensification of the global water cycle: Review and synthesis. *J. Hydrol.*, **319**, 83–95, https://doi.org/10.1016/j.jhydrol.2005.07.003.

Iguchi, T., 2020: Dual-frequency Precipitation Radar (DPR) on the Global Precipitation Measurement (GPM) mission's core observatory. *Satellite Precipitation Measurement: Volume 1*, V. Levizzani et al., Eds., Advances in Global Change Research, Vol. 67, Springer, 183–192, https://doi.org/10.1007/978-3-030-24568-9_11.

——, and Coauthors, 2022: GPM/DPR Level-2. Algorithm Theoretical Basis Doc., 238 pp., https://gpm.nasa.gov/sites/default/files/2022-06/ATBD_DPR_V07A.pdf.

IPCC, 2021: *Climate Change 2021: The Physical Science Basis.* 1st ed. Cambridge University Press, 2391 pp., https://doi.org/10.1017/9781009157896.

——, 2022: *Climate Change 2022: Impacts, Adaptation and Vulnerability*. Cambridge University Press, 3056 pp., https://doi.org/10.1017/9781009325844.

Iwabuchi, H., M. Saito, Y. Tokoro, N. S. Putri, and M. Sekiguchi, 2016: Retrieval of radiative and microphysical properties of clouds from multispectral infrared measurements. *Prog. Earth Planet. Sci.*, **3**, 32, https://doi.org/10.1186/s40645-016-0108-3.

Kida, S., S. Shige, T. Kubota, K. Aonashi, and K. Okamoto, 2009: Improvement of rain/no-rain classification methods for microwave radiometer observations over the ocean using a 37 GHz emission signature. *J. Meteor. Soc. Japan*, **87A**, 165–181, https://doi.org/10.2151/jmsj.87A.165.

——, T. Kubota, S. Shige, and T. Mega, 2018: Development of a rain/no-rain classification method over land for the microwave sounder algorithm. *Remote Sensing of Aerosols, Clouds, and Precipitation*, T. Islam et al., Eds., Elsevier, 249–265, https://doi.org/10.1016/B978-0-12-810437-8.00012-8.

Kidd, C., 1998: On rainfall retrieval using polarization-corrected temperatures. *Int. J. Remote Sens.*, **19**, 981–996, https://doi.org/10.1080/014311698215829.

——, and V. Levizzani, 2011: Status of satellite precipitation retrievals. *Hydrol. Earth Syst. Sci.*, **15**, 1109–1116, https://doi.org/10.5194/hess-15-1109-2011.

——, J. Tan, P.-E. Kirstetter, and W. A. Petersen, 2018: Validation of the version 05 Level 2 precipitation products from the GPM core observatory and constellation satellite sensors. *Quart. J. Roy. Meteor. Soc.*, **144**, 313–328, https://doi.org/10.1002/qj.3175.

——, G. Huffman, V. Maggioni, P. Chambon, and R. Oki, 2021: The global satellite precipitation constellation: Current status and future requirements. *Bull. Amer. Meteor. Soc.*, **102**, E1844–E1861, https://doi.org/10.1175/BAMS-D-20-0299.1.

Klotz, B. W., and E. W. Uhlhorn, 2014: Improved stepped frequency microwave radiometer tropical cyclone surface winds in heavy precipitation. *J. Atmos. Oceanic Technol.*, **31**, 2392–2408, https://doi.org/10.1175/JTECH-D-14-00028.1.

Kummerow, C., and L. Giglio, 1994: A passive microwave technique for estimating rainfall and vertical structure information from space. Part I: Algorithm description. *J. Appl. Meteor.*, **33**, 3–18,

https://doi.org/10.1175/1520-0450(1994)033<0003:APMTFE>2.0.CO;2.

Kummerow, C. D., 2020: Introduction to passive microwave retrieval methods. *Satellite Precipitation Measurement: Volume 1*, V. Levizzani et al., Eds., Advances in Global Change Research, Vol. 67, Springer International Publishing, 123–140, https://doi.org/10.1007/978-3-030-24568-9_7.

——, S. Ringerud, J. Crook, D. Randel, and W. Berg, 2011: An observationally generated a priori database for microwave rainfall retrievals. *J. Atmos. Oceanic Technol.*, **28**, 113–130, https://doi.org/10.1175/2010JTECHA1468.1.

——, D. L. Randel, M. Kulie, N.-Y. Wang, R. Ferraro, S. Joseph Munchak, and V. Petkovic, 2015: The evolution of the Goddard profiling algorithm to a fully parametric scheme. *J. Atmos. Oceanic Technol.*, **32**, 2265–2280, https://doi.org/10.1175/JTECH-D-15-0039.1.

Lebsock, M. D., T. S. L'Ecuyer, and G. L. Stephens, 2011: Detecting the ratio of rain and cloud water in low-latitude shallow marine clouds. *J. Appl. Meteor. Climatol.*, **50**, 419–432, https://doi.org/10.1175/2010JAMC2494.1.

Lee, Y.-R., D.-B. Shin, J.-H. Kim, and H.-S. Park, 2015: Precipitation estimation over radar gap areas based on satellite and adjacent radar observations. *Atmos. Meas. Tech.*, **8**, 719–728, https://doi.org/10.5194/amt-8-719-2015.

Lensky, I. M., and D. Rosenfeld, 2008: Clouds-Aerosols-Precipitation Satellite Analysis Tool (CAPSAT). *Atmos. Chem. Phys.*, **8**, 6739–6753, https://doi.org/10.5194/acp-8-6739-2008.

Levizzani, V., J. Schmetz, H. J. Lutz, J. Kerkmann, P. P. Alberoni, and M. Cervino, 2001: Precipitation estimations from geostationary orbit and prospects for METEOSAT Second Generation. *Meteor. Appl.*, **8**, 23–41, https://doi.org/10.1017/S1350482701001037.

Liao, L., and R. Meneghini, 2019: Physical evaluation of GPM DPR single- and dual-wavelength algorithms. *J. Atmos. Oceanic Technol.*, **36**, 883–902, https://doi.org/10.1175/JTECH-D-18-0210.1.

Lin, X., and A. Y. Hou, 2012: Estimation of rain intensity spectra over the continental United States using ground radar–gauge measurements. *J. Climate*, **25**, 1901–1915, https://doi.org/10.1175/JCLI-D-11-00151.1.

Liu, C., and E. J. Zipser, 2009: "Warm rain" in the tropics: Seasonal and regional distributions based on 9 yr of TRMM data. *J. Climate*, **22**, 767–779, https://doi.org/10.1175/2008JCLI2641.1.

Lorenz, C., and H. Kunstmann, 2012: The hydrological cycle in three state-of-the-art reanalyses: Intercomparison and performance analysis. *J. Hydrometeor.*, **13**, 1397–1420, https://doi.org/10.1175/JHM-D-11-088.1.

Maggioni, V., P. C. Meyers, and M. D. Robinson, 2016: A review of merged high-resolution satellite precipitation product accuracy during the Tropical Rainfall Measuring Mission (TRMM) era. *J. Hydrometeor.*, **17**, 1101–1117, https://doi.org/10.1175/JHM-D-15-0190.1.

——, C. Massari, and C. Kidd, 2022: Errors and uncertainties associated with quasiglobal satellite precipitation products. *Precipitation Science*, S. Michaelides, Ed., Elsevier, 377–390, https://doi.org/10.1016/B978-0-12-822973-6.00023-8.

Masaki, T., T. Iguchi, K. Kanemaru, K. Furukawa, N. Yoshida, T. Kubota, and R. Oki, 2020: Calibration of the dual-frequency precipitation radar onboard the global precipitation measurement core observatory. *IEEE Trans. Geosci. Remote Sens.*, **60**, 1–16, https://doi.org/10.1109/TGRS.2020.3039978.

Matrosov, S. Y., and D. D. Turner, 2018: Retrieving mean temperature of atmospheric liquid water layers using microwave radiometer measurements. *J. Atmos. Oceanic Technol.*, **35**, 1091–1102, https://doi.org/10.1175/JTECH-D-17-0179.1.

McCollum, J. R., W. F. Krajewski, R. R. Ferraro, and M. B. Ba, 2002: Evaluation of biases of satellite rainfall estimation algorithms over the continental United States. *J. Appl. Meteor. Climatol.*, **41**, 1065–1080, https://doi.org/10.1175/1520-0450(2002)041<1065:EOBOSR>2.0.CO;2.

Munchak, S. J., and G. Skofronick-Jackson, 2013: Evaluation of precipitation detection over various surfaces from passive microwave imagers and sounders. *Atmos. Res.*, **131**, 81–94, https://doi.org/10.1016/j.atmosres.2012.10.011.

Muñoz-Sabater, J., and Coauthors, 2021: ERA5-Land: A state-of-the-art global reanalysis dataset for land applications. *Earth Syst. Sci. Data*, **13**, 4349–4383, https://doi.org/10.5194/essd-13-4349-2021.

Nath, P. K., and B. Behera, 2011: A critical review of impact of and adaptation to climate change in developed and developing economies. *Environ. Dev. Sustainability*, **13**, 141–162, https://doi.org/10.1007/s10668-010-9253-9.

Overeem, A., T. A. Buishand, and I. Holleman, 2009a: Extreme rainfall analysis and estimation of depth-duration-frequency curves using weather radar. *Water Resour. Res.*, **45**, W10424, https://doi.org/10.1029/2009WR007869.

——, I. Holleman, and A. Buishand, 2009b: Derivation of a 10-year radar-based climatology of rainfall. *J. Appl. Meteor. Climatol.*, **48**, 1448–1463, https://doi.org/10.1175/2009JAMC1954.1.

——, H. Leijnse, and R. Uijlenhoet, 2011: Measuring urban rainfall using microwave links from commercial cellular communication networks. *Water Resour. Res.*, **47**, W12505, https://doi.org/10.1029/2010WR010350.

Panegrossi, G., A. C. Marra, P. Sanò, L. Baldini, D. Casella, and F. Porcù, 2020: Heavy precipitation systems in the Mediterranean area: The role of GPM. *Satellite Precipitation Measurement: Volume 2*, V. Levizzani et al., Eds., Advances in Global Change Research, Vol. 69, Springer International Publishing, 819–841, https://doi.org/10.1007/978-3-030-35798-6_18.

Pedregosa, F., and Coauthors, 2011: Scikit-learn: Machine learning in Python. *J. Mach. Learn. Res.*, **12**, 2825–2830.

Petković, V., C. D. Kummerow, D. L. Randel, J. R. Pierce, and J. K. Kodros, 2018: Improving the quality of heavy precipitation estimates from satellite passive microwave rainfall retrievals. *J. Hydrometeor.*, **19**, 69–85, https://doi.org/10.1175/JHM-D-17-0069.1.

——, M. Orescanin, P. Kirstetter, C. Kummerow, and R. Ferraro, 2019: Enhancing PMW satellite precipitation estimation: Detecting convective class. *J. Atmos. Oceanic Technol.*, **36**, 2349–2363, https://doi.org/10.1175/JTECH-D-19-0008.1.

Petty, G. W., and K. Li, 2013: Improved passive microwave retrievals of rain rate over land and ocean. Part I: Algorithm description. *J. Atmos. Oceanic Technol.*, **30**, 2493–2508, https://doi.org/10.1175/JTECH-D-12-00144.1.

——, and R. Bennartz, 2017: Field-of-view characteristics and resolution matching for the Global Precipitation Measurement (GPM) Microwave Imager (GMI). *Atmos. Meas. Tech.*, **10**, 745–758, https://doi.org/10.5194/amt-10-745-2017.

Randel, D. L., C. D. Kummerow, and S. Ringerud, 2020: The Goddard Profiling (GPROF) precipitation retrieval algorithm. *Satellite Precipitation Measurement: Volume 1*, V. Levizzani et al., Eds., Advances in Global Change Research, Vol. 67, Springer International Publishing, 141–152, https://doi.org/10.1007/978-3-030-24568-9_8.

Saltikoff, E., and Coauthors, 2019: An overview of using weather radar for climatological studies: Successes, challenges, and potential. *Bull. Amer. Meteor. Soc.*, **100**, 1739–1752, https://doi.org/10.1175/BAMS-D-18-0166.1.

Segal, M. R., 2004: Machine learning benchmarks and random forest regression. 14 pp., https://escholarship.org/content/qt35x3v9t4/qt35x3v9t4_noSplash_3bc7fbb8348b76e0ad2a408fe58dfd94.pdf.

Shen, Z., and Coauthors, 2020: Recent global performance of the Climate Hazards group Infrared Precipitation (CHIRP) with Stations (CHIRPS). *J. Hydrol.*, **591**, 125284, https://doi.org/10.1016/j.jhydrol.2020.125284.

Shige, S., S. Kida, H. Ashiwake, T. Kubota, and K. Aonashi, 2013: Improvement of TMI rain retrievals in mountainous areas. *J. Appl. Meteor. Climatol.*, **52**, 242–254, https://doi.org/10.1175/JAMC-D-12-074.1.

Skofronick-Jackson, G., W. Berg, C. Kidd, D. B. Kirschbaum, W. A. Petersen, G. J. Huffman, and Y. N. Takayabu, 2018: Global Precipitation Measurement (GPM): Unified precipitation estimation from space. *Remote Sensing of Clouds and Precipitation*, C. Andronache, Ed., Springer Remote Sensing/Photogrammetry, Springer International Publishing, 175–193, https://doi.org/10.1007/978-3-319-72583-3_7.

Spencer, R. W., 1986: A satellite passive 37-GHz scattering-based method for measuring oceanic rain rates. *J. Climate Appl. Meteor.*, **25**, 754–766, https://doi.org/10.1175/1520-0450(1986)025<0754:ASPGSB>2.0.CO;2.

Stephens, G. L., and C. D. Kummerow, 2007: The remote sensing of clouds and precipitation from space: A review. *J. Atmos. Sci.*, **64**, 3742–3765, https://doi.org/10.1175/2006JAS2375.1.

Tang, G., M. P. Clark, S. M. Papalexiou, Z. Ma, and Y. Hong, 2020: Have satellite precipitation products improved over last two decades? A comprehensive comparison of GPM IMERG with nine satellite and reanalysis datasets. *Remote Sens. Environ.*, **240**, 111697, https://doi.org/10.1016/j.rse.2020.111697.

Tiberia, A., and Coauthors, 2021: GPM-DPR observations on TGFs producing storms. *J. Geophys. Res. Atmos.*, **126**, e2020JD033647, https://doi.org/10.1029/2020JD033647.

Toyoshima, K., H. Masunaga, and F. A. Furuzawa, 2015: Early evaluation of Ku- and Ka-band sensitivities for the Global Precipitation Measurement (GPM) Dual-Frequency Precipitation Radar (DPR). *SOLA*, **11**, 14–17, https://doi.org/10.2151/sola.2015-004.

Turk, F. J., and Coauthors, 2021: Adapting passive microwave-based precipitation algorithms to variable microwave land surface emissivity to improve precipitation estimation from the GPM constellation. *J. Hydrometeor.*, **22**, 1755–1781, https://doi.org/10.1175/JHM-D-20-0296.1.

Watters, D., A. Battaglia, K. Mroz, and F. Tridon, 2018: Validation of the GPM version-5 surface rainfall products over Great Britain and Ireland. *J. Hydrometeor.*, **19**, 1617–1636, https://doi.org/10.1175/JHM-D-18-0051.1.

Weng, F., and N. C. Grody, 2000: Retrieval of ice cloud parameters using a microwave imaging radiometer. *J. Atmos. Sci.*, **57**, 1069–1081, https://doi.org/10.1175/1520-0469(2000)057<1069:ROICPU>2.0.CO;2.

Wilheit, T., and Coauthors, 1994: Algorithms for the retrieval of rainfall from passive microwave measurements. *Remote Sens. Rev.*, **11**, 163–194, https://doi.org/10.1080/02757259409532264.

Wilheit, T. T., A. T. C. Chang, M. S. V. Rao, E. B. Rodgers, and J. S. Theon, 1977: A satellite technique for quantitatively mapping rainfall rates over the oceans. *J. Appl. Meteor.*, **16**, 551–560, https://doi.org/10.1175/1520-0450(1977)016<0551:ASTFQM>2.0.CO;2.

——, and Coauthors, 1982: Microwave radiometric observations near 19.35, 92 and 183 GHz of precipitation in tropical storm Cora. *J. Appl. Meteor.*, **21**, 1137–1145, https://doi.org/10.1175/1520-0450(1982)021<1137:MRONAG>2.0.CO;2.

Winsemius, H. C., B. Jongman, T. I. E. Veldkamp, S. Hallegatte, M. Bangalore, and P. J. Ward, 2018: Disaster risk, climate change, and poverty: Assessing the global exposure of poor people to floods and droughts. *Environ. Dev. Econ.*, **23**, 328–348, https://doi.org/10.1017/S1355770X17000444.

Wolfensberger, D., M. Gabella, M. Boscacci, U. Germann, and A. Berne, 2021: RainForest: A random forest algorithm for quantitative precipitation estimation over Switzerland. *Atmos. Meas. Tech.*, **14**, 3169–3193, https://doi.org/10.5194/amt-14-3169-2021.

Yamamoto, M. K., S. Shige, C.-K. Yu, and L.-W. Cheng, 2017: Further improvement of the heavy orographic rainfall retrievals in the GSMaP algorithm for microwave radiometers. *J. Appl. Meteor. Climatol.*, **56**, 2607–2619, https://doi.org/10.1175/JAMC-D-16-0332.1.

You, Y., and Coauthors, 2020: Raindrop signature from microwave radiometer over deserts. *Geophys. Res. Lett.*, **47**, e2020GL088656, https://doi.org/10.1029/2020GL088656.